Supplementary Materials

Stability of Optical Knots in Atmospheric Turbulence

D. G. Pires[†], D. Tsvetkov[†], H. Barati Sedeh, N. Chandra, and N. M. Litchinitser[*]

Department of Electrical and Computer Engineering, Duke University, Durham, North Carolina 27708, USA

S1. Turbulence chamber: calibration and using uncorrelated phase screens

The turbulence chamber utilized for the experiments shown in the main manuscript consists of a $150 \times 150 \times 150$ mm internal mixing volume, having two fans for room-temperature air intake, one for heated air intake, and another for exhaust. As the optical beam passes through the input and output ports, it acquires a dynamic phase distortion due to the turbulent airflow inside the chamber. The maximum temperature of the heated air is 120 ℃, with a stability of approximately ± 0.1 ℃. The transverse airflow can achieve a Greenwood frequency of about $f_G = 35$ Hz. To match the turbulence levels in both experiments and simulations, we calibrate the system by measuring the scintillation index of a Gaussian beam with respect to the chamber's temperature. This index is then compared to the scintillation index in simulations for multiple Rytov variance values. Figure S1 (a) shows the calibration curve, which agrees with the numerical simulation predictions. The scintillation index $\sigma_I^2 = \langle I^2(\mathbf{0})\rangle / \langle I(\mathbf{0})\rangle^2 - 1$ is calculated by measuring the on-axis intensity values of a Gaussian beam propagating through the turbulence link. For each realization, we average the intensity values within the nine central pixels for both numerical and experimental evaluations. Here, 2000 different realizations were performed.

Using a realistic, time-dependent turbulence chamber might lead to challenges when performing phase measurements, which rely on acquiring a few interferograms to retrieve the complex field distribution. To explain the small discrepancy with respect to the numerical simulations, which consider a static turbulent medium and/or superfast measurement techniques,

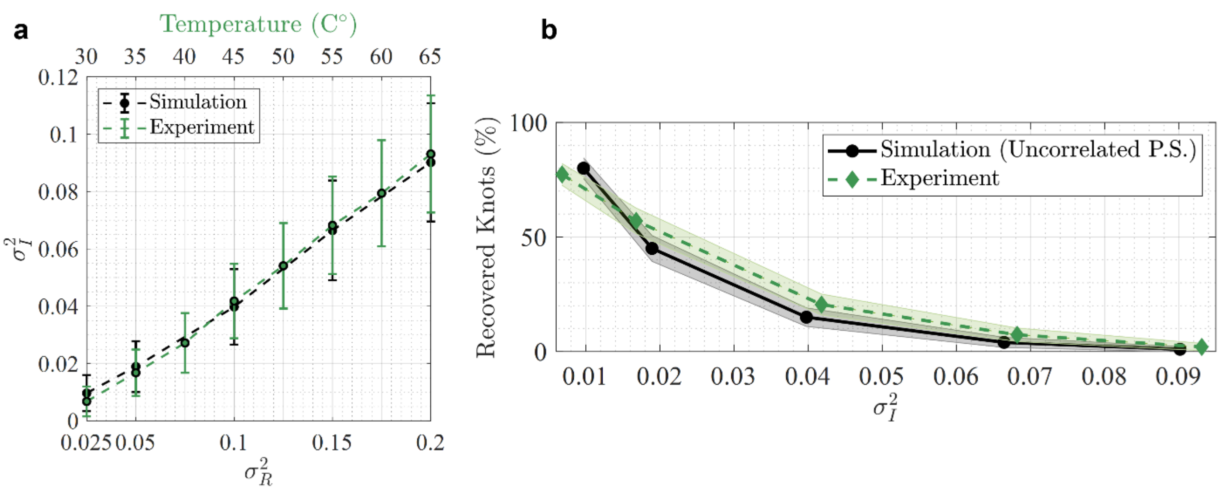

Fig. S1. a. Calibration curve, with their respective propagated errors based on the mean squared errors, for the experimental turbulence chamber with respect to the scintillation values numerically calculated, using 2000 different realizations for both experiments and simulations. **b.** Percentage of recovered trefoils, where the black dots correspond to the numerical simulation using uncorrelated phase screens in between the three-step frame technique to acquire the complex field distribution. The green diamonds show the same experimental results presented in the main manuscript.

we performed additional calculations considering totally uncorrelated phase screens while acquiring the three required interferograms to reconstruct the optical field (see Methods for details on the three-step frame technique). Here, we use three different propagations to numerically recreate the temporal dynamics of the chamber and construct the three interferograms, just as in the experimental case. Figure S1 (b) clarifies that the SLM frame rate, which is about 60 Hz for one hologram switch, is
not fast enough to overcome the temporal changes of the refractive index inside the turbulence chamber. One could overcome the frame rate challenges by using faster holographic devices such as DMD or acoustic-optical deflectors (AOD), which can achieve frame rates of about 32 kHz and 400 kHz, respectively.

To estimate the refractive index structure parameter C_n^2 of the experimental system, we relied on statistical measurements from the beam wandering of a Gaussian beam. Such a relationship is given by $C_n^2 = 0.328\langle r_c^2\rangle D^{1/3}L^{-3}$, where D is the beam diameter, L is the turbulence link length, and $\langle r_c^2\rangle = \langle x^2\rangle + \langle y^2\rangle$ is the variance of the beam wander displacement on the detector [S1]. The curves showing the experimentally estimated C_n^2 using 2000 different realizations, alongside the numerical values, are shown in Fig. S2 (a). The Fried parameter r_0 can be determined by the relation $r_0 = 1.68(C_n^2 L k^2)^{-3/5}$, with the wavenumber $k = 2\pi/\lambda$ already introduced in the main text. Figure S2 (b) depicts the curve with the experimental estimations for r_0, superposed with the numerical counterparts. Notice that our laboratory scale experimental setup was carefully designed to mimic a realistic free-space optical link based on a $w_0 = 6$ mm beam propagating over a $L = 270$ m distance [S2], making use of the Fresnel scaling to ensure the same optical properties in both scenarios. In particular, to simulate similar values of scintillations in simulations and experiments, stronger turbulence had to be realized while using the hot air chamber to compensate for the shorter propagation distance and smaller beam size. For instance, simply using the mathematical expression for the Rytov variance $\sigma_R^2 = 1.23 C_n^2 k^{7/6} L^{11/6}$ to estimate the order of magnitude of C_n^2 for such shorter propagation distance, here $L_{\text{lab}} = 1.5$ m, gives the same order of magnitude we observe in Fig. S2 (a).

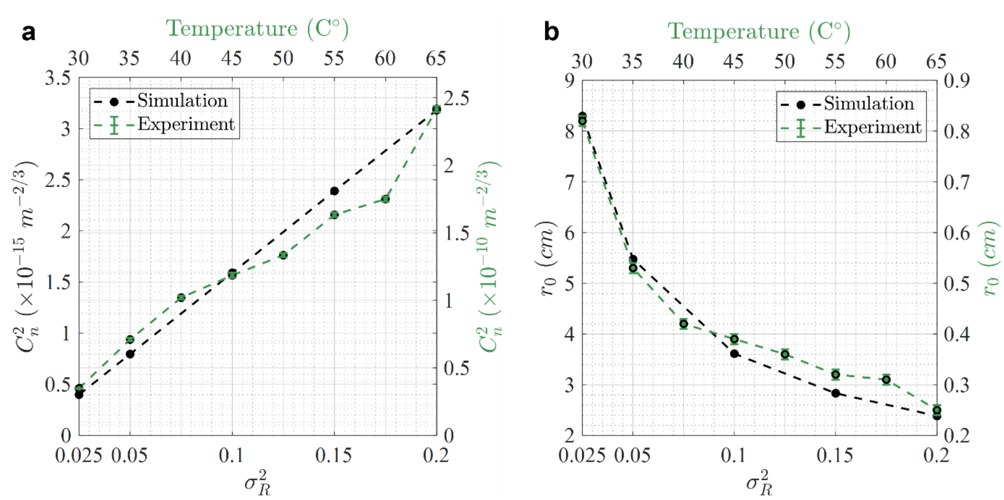

Fig. S2. a Experimental estimation of the refractive index structure parameter C_n^2 with respect to temperature values of the turbulence chamber (green), together with the parameter used in the simulations (black) with respect to the Rytov variance σ_R^2. Here, 2000 experimental realizations were performed, and the error bars correspond to the mean squared error. **b** The respective Fried parameter r_0 values for both simulations (black) and experiments (green) are similar to panel **(a)**.

S2. Trefoil Knot

Following the procedure outlined in Supplementary Ref. [S3], the Milnor polynomial for a trefoil knot can be written as

$$f_{\text{trefoil}}(R,\phi,z)=\left\{(R^4-1)(R^2-1)-8R^3e^{3i\phi}\right\}+4iz(R^4-1)$$
$$+z^2(3R^4-6R^2-5)+8iz^3R^2+z^4(3R^2-5)+4iz^5+z^6. \tag{S1}$$

To derive the expression for the optical trefoil knot used in both experimental studies and numerical simulations, we first set $z=0$ in Eq. (S1) (see Fig. S3 (a)). Next, we multiply this expression by the Gaussian envelope given by $\mathrm{LG}_{0,0}(R,\phi,0)=e^{-R^2/2w^2}/\left(w\sqrt{\pi}\right)$ and obtain

$$F_{\text{trefoil}}(R,\phi,0)=\frac{(R^4-1)(R^2-1)-8R^3e^{3i\phi}}{w\sqrt{\pi}}e^{-\frac{R^2}{2w^2}}. \tag{S2}$$

Figures S3 (b-f) show that as the envelope width parameter w increases, the positions of singularities stay the same, but the intensity distributions around the singularities change. By projecting Eq. (S2) onto the LG basis, we can find the coefficients $c_{p,l}(w)$ in Eq. (1) of the main text.

$$\mathrm{LG}_{p,l}(R,\phi,z)=\sqrt{\frac{p!}{\pi(|l|+p)!}}\frac{R^{|l|}e^{il\phi}}{w_0^{|l|+1}}\frac{(1-iz/z_R)^p}{(1+iz/z_R)^{p+|l|+1}}$$
$$e^{-\frac{R^2}{2w_0^2(1+iz/z_R)}}L_p^{|l|}\left(\frac{R^2}{w_0^2(1+z^2/z_R^2)}\right). \tag{S3}$$

Here, $z_R=kw_0^2$ is the Rayleigh length, and $L_p^{|l|}$ is the associated Laguerre polynomial. Note that in general, different $\mathrm{LG}_{p,l}$ modes can have different waists $w_{0_{p,l}}$, and in this case, $w_{0_{p,l}}$ can potentially be used as additional parameters to control the relative positions of the singularities. Even though w_0 is not necessarily equal to w in Eq. (S2), for simplicity, here we set $w_0=w$. Consequently, the coefficients $c_{p,l}(w)$ corresponding to a particular $\mathrm{LG}_{p,l}$ mode in the superposition can be determined from

$$\overbrace{1-w^2-2w^4+6w^6}^{(p,l)=(0,0)}\Bigg|\overbrace{w^2(1+4w^2-18w^4)}^{(1,0)}\Bigg|\overbrace{-2w^4(1-9w^2)}^{(2,0)}\Bigg|\overbrace{-6w^6}^{(3,0)}\Bigg|\overbrace{-8\sqrt{6}w^3}^{(0,3)}, \tag{S4}$$

where (p,l) are the LG mode indices. Throughout this work, we normalize the coefficients in Eq. S4, so the sum of squares is equal to 100, but since the knotted field is simply a mode superposition, one could use any normalization as long as the relative weightings between the modes are the same. It is important to note that w the parameter is not identical to the final beam waist of the LG

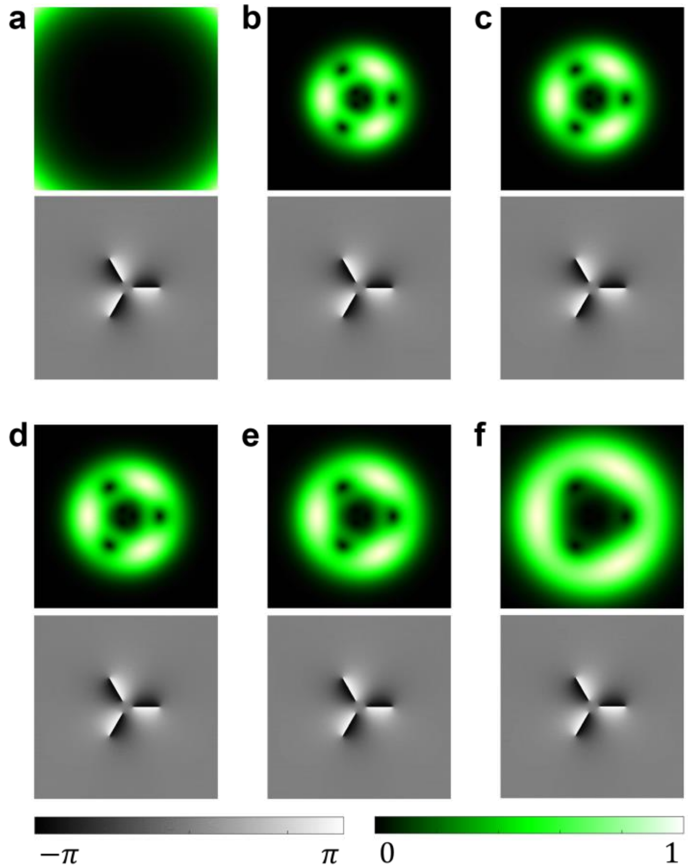

Fig. S3. Amplitude and phase distributions for (**a**) the Milnor polynomial expression in Eq. S1 and (**b**-**f**) after including the Gaussian envelope with different widths w at $z = 0$ (**b**) $w = 1$, (**c**) $w = 1.05$, (**d**) $w = 1.1$, (**e**) $w = 1.2$, and (**f**) $w = 1.5$.

beams in Eq. (1). While the parameter w dictates the intensity distribution around the singularity lines, the LG beam waist w_0 in Eq. (1) defines the size of each constitutive $\mathrm{LG}_{p,l}$ mode, and subsequently, the entire beam. Figure S3 (b-f) shows the amplitude and phase distributions for different values of w with the beam waist $w_0 = w$. They are identical to the ones obtained from Eq. (S2).

S3. Trefoil Knot Coefficients

The value for the parameter w that performs optimally in the presence of turbulence must be chosen, as this parameter dictates how isolated the knotted structure is from the outer singularities [S3]. The beam waist w_0 was kept constant in this study. For $\sigma_R = 0.025$ and $\sigma_R = 0.05$, we found that $w = 1.15$ leads to the best stability of the knot in turbulence, as shown in Fig. S4 (f). When

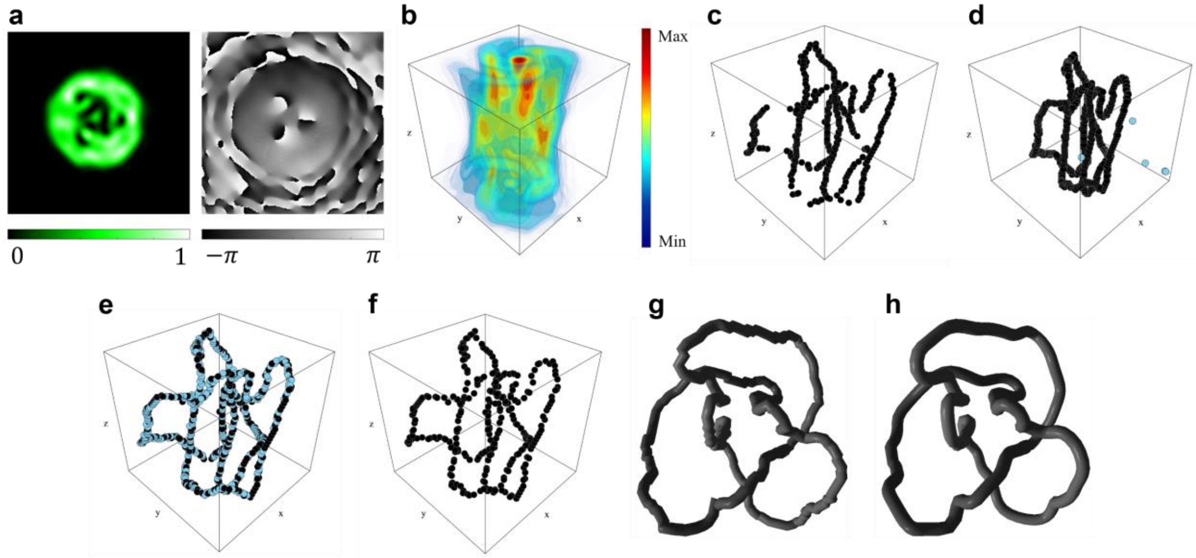

Fig. S5. **a** Experimentally measured intensity and phase distribution of a trefoil knot. **b** Intensity distribution after post- and back-propagating the measured optical field. **c** Phase singularities at *the x-y* cross-section at every longitudinal position. **d** Phase singularities after scanning the *x-z* and *y-z* cross-sections. **e** Recovered singularities with chosen dots highlighted (blue) to be discarded to increase the efficiency of the algorithm. **f** Resulting knotted structure after removing the dots highlighted in panel (**e**). **g** Trefoil knot after using a Traveling Salesman problem to predict the correct singularity trajectory. **h** Final structure after interpolation to smooth the measured phase singularity trajectories.

$w < 1.15$, the outer singularities move closer to the isolated knot, and the probability of the singularity lines reconnection in turbulence increases. Even though setting $w > 1.15$ results in a completely isolated knot, the overall knotted structure becomes small, thereby increasing the probability of a reconnection event occurring inside the knot. Even though the Gaussian envelope width w directly affects the performance of the trefoil knot without being optimized, it is worth mentioning that the optimization algorithm described in the main text leads to the same field superposition regardless of the initial value of w.

S4. Measuring optical knots in turbulence

Figure S5 summarizes the steps for the reconstruction of the 3D knot from experimental data. Following the measurement of the complex field (shown in Fig. S5 (a)) in a particular plane $z = 0$ (in the middle of the Rayleigh length $z_R = kw_0^2$), we numerically propagate this field in the positive and negative z-direction using an angular spectrum algorithm [S4]. Note that the developed procedure can be used to reconstruct the 3D knot from any plane, *i.e.*, not necessarily from the plane corresponding to $z = 0$. The 3D intensity resulting from this reconstruction procedure is shown in Fig. S5 (b). The singularities in the *x-y* plane are found by determining the points corresponding to $\mathrm{Re}\{E\} = \mathrm{Im}\{E\} = 0$, where E is the complex field at every longitudinal position. Figure S5 (c) shows the reconstructed knotted structure. To further improve the precision

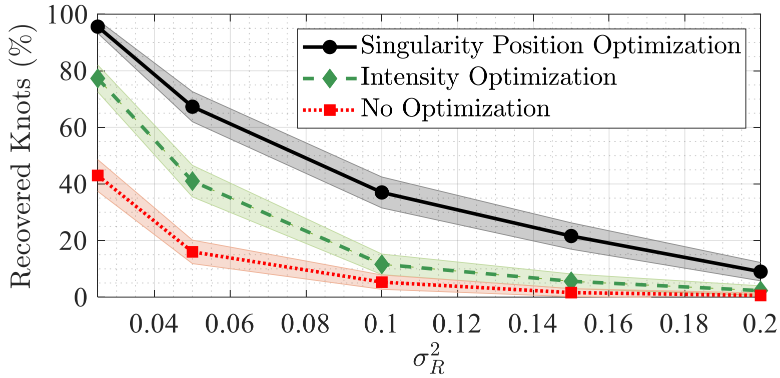

Fig. S6. Numerically simulated results inferring the percentage of recovered trefoils after propagating through a turbulent path with multiple strength levels, here denoted as Rytov variance. Black dots indicate the results where the singularity position optimization was used, green diamonds refer to the intensity optimization, and red squares to the case where no optimization were performed. The shadowed regions denote the 95% confidence interval.

of finding the locations of the singularities, we repeat the same procedure and search for the singularities in the *x-z* and *y-z* cross-sections, as shown in Fig. S5 (d). Because the mesh is finite, the position of singularities obtained from different planes may yield slightly different coordinates. This results in multiple, closely spaced points of singularities along the same singularity line (as shown in Fig. S5 (e)). Therefore, we are discarding some of these points to reduce the density of dots, thereby accelerating subsequent steps. The resulting knot is shown in Fig. S5 (f). Now, we establish the correct trajectory of the retrieved singularities using the Traveling Salesman problem, leading to the structure in Fig. S5 (g). Finally, in Fig. S5 (h), interpolation is applied using a polynomial approximation to smooth out the overall singularity lines.

S5. Mathematical trefoil knot compared to the optimization processes

To fully compare the importance of optimizing the coefficients of the optical modes encoded into the beam, in Fig. S6, we present the numerically simulated results for the propagation of the knotted beam without any optimization together with the ones where an optimization process was realized. The black dots represent the singularity position optimization, the green diamonds correspond to the intensity optimization, and the red squares denote the case where no optimization was done. As discussed in the main manuscript, we found that maximizing the intensity contrast together with maximizing the distance between the singularities leads to better stability against external perturbations.

S6. Spectrum broadening due to turbulence and reconnection events

While interacting with turbulence, the superposition of modes composing the knotted field experiences collective crosstalk, meaning that additional LG modes carrying specific radial and azimuthal modes (l and p, respectively) are included in the overall complex field. In Fig. S7 (a-c), we observe the LG spectrum after the trefoil knot interacts with the turbulence of Rytov variance $\sigma_R^2 = 0.15$ for the cases where (a) it maintains the trefoil topology, (b) it transforms into a Hopf link, and (c) it changes to an unknot. The color bar refers to the absolute value of each amplitude weighting $c_{p,l}$ within the complex field. As the initial trefoils transition into a Hopf or an unknot, the more crosstalk the composing optical modes suffer due to turbulence.

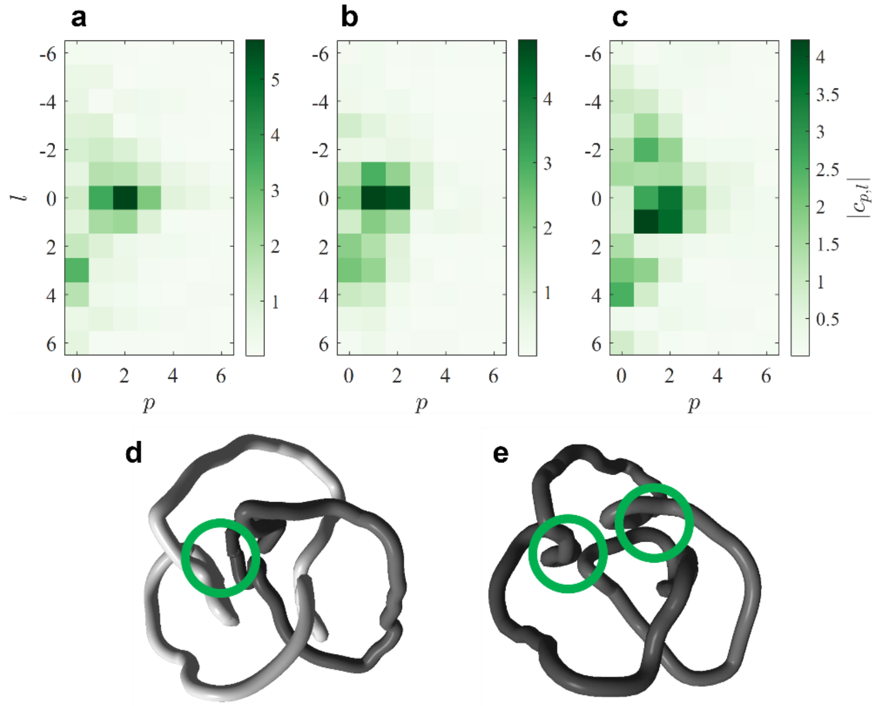

Fig. S7. Laguerre-Gaussian spectrum distribution for an initial optical trefoil knot which (**a**) maintained its shape, (**b**) transitioned into a Hopf link, and (**c**) changed into an unknot. Here, the Rytov variance were $\sigma_R^2 = 0.15$. **d,e** Examples of reconnection events where the trefoil changed into a Hopf link and an unknot, respectively. The green circles highlight the location where the singularity lines reconnected and changed the initial topology.

These transitions from trefoil knot to Hopf link or unknot are observed through reconnection events, as pointed in Fig. S7 (d,e). The green circles highlight the location where the reconnection events happened for the case where the trefoil changed into a (d) Hopf link and (e) to an unknot. Only one reconnection event is necessary for a trefoil knot transition into a Hopf link, while two reconnections are needed for it to change into an unknot. It is worth mentioning that, due to the dynamic and statistical nature of turbulence, each realization reported throughout this manuscript presents a slightly different LG spectrum distribution. It is noteworthy that closed vortex lines may form during light propagation in any complex media [S5]. They result from the modal spectrum broadening upon interaction with the environment, e.g., turbulence [S6]. In particular, such a phenomenon is observed in our work and reveals itself in the reconnection events, where the addition or redistribution of optical modes resulting from the interactions with the environment leads to a change in the vortex line trajectories. The knotted vortex trajectories presented in this work differ from environmental-generated knots as they are mathematically designed to possess specific topological properties and shapes, contrasting with spontaneously generated closed vortex trajectories.

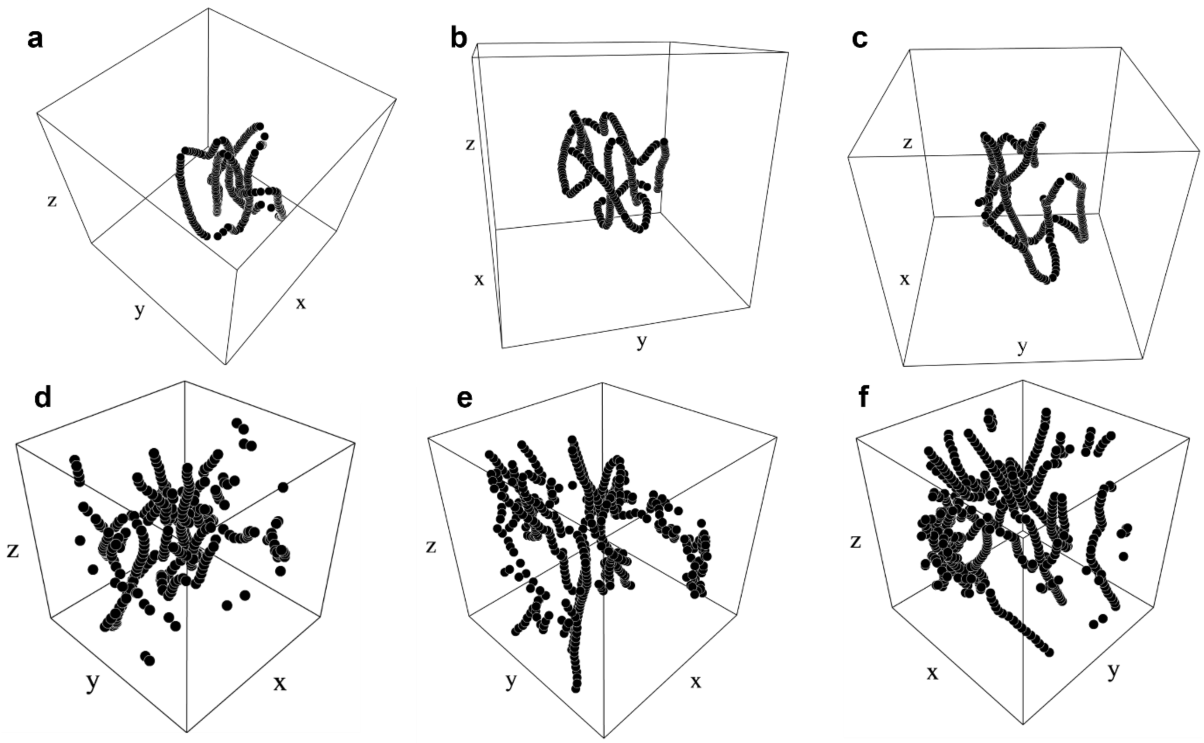

Fig. S8. Examples of (**a**) trefoil, (**b**) Hopf, (**c**) unknot, and (**d-f**) destroyed structures from experiments using the chamber after interaction with turbulence of scintillation index (**a-c**) $\sigma_I^2 = 0.007$ and (**d-f**) $\sigma_I^2 = 0.09$.

S7. More examples of recovered topologies

Figure S8 presents additional examples of measured trefoil knots, Hopf links, unknots, and cases where the knotted structures are completely destroyed after interactions with turbulence. It is important to note that these obliterated topological structures are a combination of one or more unknots and/or extra singularity lines, which reconnect to those associated with the Gaussian envelope extending from $-\infty$ to ∞ (refer to Section S3 and Fig. S2). This reconnection occurs due to turbulence, leading to the loss of the original topological information. In this work, we have classified these destroyed structures as unknots.

Additionally, amplitude and phase distributions of the measured knotted field using the turbulence chamber for multiple temperature settings are shown in Fig. S9. Here, 3 different realizations are plotted for temperature (scintillation) values of (a) $T = 30$ ℃ ($\sigma_I^2 = 0.0068$), (b) $T = 45$ ℃ ($\sigma_I^2 = 0.0418$), and (c) $T = 65$ ℃ ($\sigma_I^2 = 0.0931$). At higher turbulence strengths, more complex and smaller scale beam alterations are applied.

Figure S10 shows how tilt-like aberrations affect the knotted beams, where the amplitude and phase distributions and corresponding 3D singularity lines are shown. Here, we numerically apply tilts along the x-direction in the form of $E_{tilt} = E_0 \exp(ik_x x)$ as (a) $k_x = k_0 \times 10^{-5}$, (b) $k_x = 2.5k_0 \times 10^{-5}$, and (c) $k_x = 5k_0 \times 10^{-5}$. In all cases, the trefoil topology is maintained. Such types of aberrations correspond to the 1st order aberrations in terms of Zernike polynomials, suggesting the higher-order terms are required to substantially change the knots' topology.

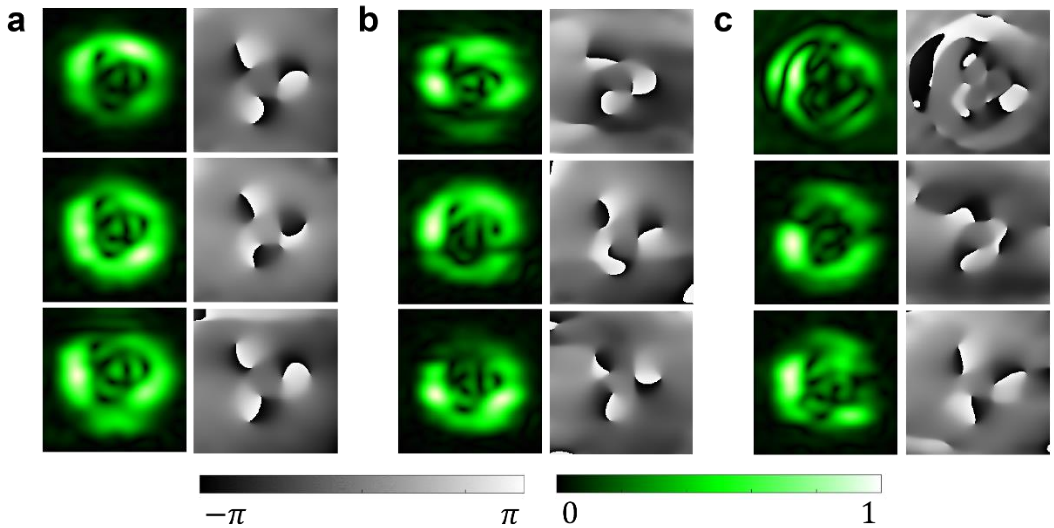

Fig. S9. Examples of amplitude and phase distributions measured at different temperature (scintillation) values in the turbulence chamber. Each row represents different realizations at (**a**) $T = 30$ ℃ ($\sigma_I^2 = 0.0068$), (**b**) $T = 45$ ℃ ($\sigma_I^2 = 0.0418$), and (**c**) $T = 65$ ℃ ($\sigma_I^2 = 0.0931$).

S8. Limitations of the method

The concept of the optimization process was inspired by Ref. [S3], where the authors demonstrated that a numerical adjustment of the coefficients can enhance the precision of the measurements. Comparing the modal superposition in the LG basis for knots with different topological orders (Hopf links, trefoils, cinquefoils, etc.) [S3], we notice that higher order knots are built of a superposition of a larger number of $\mathrm{LG}_{p,l}$ modes. The larger number of constitutive modes leads to more degrees of freedom for numerical optimization, and therefore, to more stable results. For this reason, we expect the singularity position optimization to be less efficient when one has a smaller number of optical modes constituting the knotted structure. The results presented in this study could potentially be further improved by adding more radial modes to the knotted field.

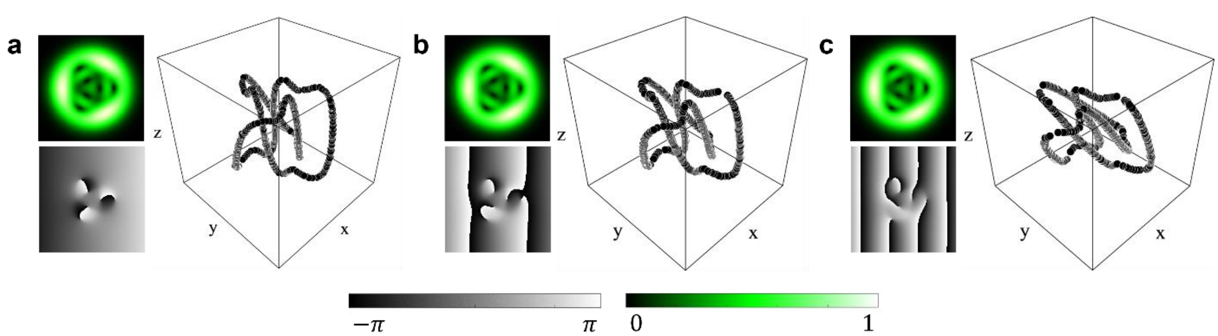

Fig. S10. Examples of tilt-like aberrations applied to the optical trefoil knot. Each tilt along the $\boldsymbol{x}$-direction has magnitude of (**a**) $k_x = k_0 \times 10^{-5}$, (**b**) $k_x = 2.5k_0 \times 10^{-5}$, and (**c**) $k_x = 5k_0 \times 10^{-5}$. The corresponding amplitudes and phase distributions, along with the resulting 3D singularity lines, are shown.

Supplementary References

S1. Andrews, L.C. and R.L. Phillips, *Laser beam propagation through random media.* Laser Beam Propagation Through Random Media: Second Edition, 2005.

S2. Peters, C., et al., *The invariance and distortion of vectorial light across a real-world free space link.* Applied Physics Letters, 2023. **123**(2)

S3. Dennis, M.R., et al., *Isolated optical vortex knots.* Nature Physics, 2010. **6**(2): p. 118-121.

S4. Zhong, J.Z., et al., *Reconstructing the topology of optical vortex lines with single-shot measurement.* Applied Physics Letters, 2021. **119**(16).

S5. O'Holleran, Kevin, M. J. Padgett, and M. R. Dennis. "*Topology of optical vortex lines formed by the interference of three, four, and five plane waves*." Optics Express, 2006. **14** (7): 3039-3044.

S6. Cox, M.A., et al., *Structured Light in Turbulence*. IEEE Journal of Selected Topics in Quantum Electronics, 2021. **27**(2).